Influences of different Zr additions on the microstructure, room and high temperature mechanical properties of an Al-7Si-0.4Mg alloy modified with 0.25%Er

Marco Colombo[a,*], Elisabetta Gariboldi[a], Alessandro Morri[b]

[a] *Politecnico di Milano, Department of Mechanical Engineering, Via La Masa 1, 20156 Milan, Italy*
[b] *Department of Industrial Engineering (DIN), Alma Mater Studiorum, University of Bologna, Viale Risorgimento 4, 40136 Bologna, Italy*

In this work, three innovative age hardenable Al alloys based on the Al-7Si-0.4Mg-0.25Er system (A356 alloy + 0.25 wt% Er), with nominal additions of Zr between 0 and 0.6 wt%, are designed, cast, heat treated and char-acterized from a microstructural and mechanical point of view. Zr additions leads to a progressive reduction of the Secondary Dendrites Arm Spacing (SDAS) of the alloys, due to inoculant pro-peritectic intermetallics and growth rate restriction of dendrites during solidification, and a reduction in eutectic Si size. 0.6 wt% Zr also causes a morphological modification of dendrites, which display a globular shape, thanks to the inoculation action of primary Zr-containing intermetallics. Tensile tests performed in the peak aged and overaged conditions reveal the beneficial effect of Zr on the mechanical properties of the alloys; in particular, the alloy with the highest Zr content shows the highest mechanical properties in all the tested conditions. This work shows the potentialities of Zr as an alloying element to increase the microstructural stability and mechanical properties of Al-Si-Mg-Er alloy.

Keywords:
Al-7Si-0.4Mg (A356) alloy
Erbium, Zirconium additions
Microstructure
Inoculation
High temperature mechanical properties
Aging

1. Introduction

Considerable efforts have been made in recent years to develop innovative Al alloys characterized by improved mechanical properties and resistance to high temperature exposure, two critical aspects preventing their wider diffusion for structural applications [1–4]. One of the fields that could greatly benefit from the development of stronger and more thermally resistant Al alloys is the transportation industry. The substitution of steel with high strength Al alloys, in fact, causes a dramatic weight reduction, with a consequent decrease in energy consumption.

Cast, age-hardenable Al-based alloys are commonly employed in transportation industry, particularly those based on the Al-Si-Mg system. This family of alloys is characterized by good mechanical properties in the heat-treated condition, good corrosion resistance and excellent castability. All these characteristics make them suitable for structural applications at room temperature, but the relatively poor thermal stability of these alloys above 423 K limits their use at higher temperature.

A common solution to widen the applicability field of Al-Si-Mg al-loys is the addition of small amounts of alloying elements, capable of forming precipitates that strengthen the material at room temperature and stabilize their microstructure, retarding the decay in mechanical properties when exposed to high temperatures. A previous study by the authors, supported by other researches published in literature, suggested that Er can effectively act as a strengthening element for Al-Si-Mg alloys both at room and elevated temperatures [5–8]. The origin of the improved mechanical and microstructural characteristics of Er-containing alloys is found in the formation of coarsening resistant nanometric Er-rich dispersoids, that retard dislocations motion [6–8].

Literature studies on pure Al demonstrated that its mechanical properties at room and high temperatures can be further improved by the joint addition of Er and Zr, thanks to the formation of nanometric core-shell dispersoids characterized by an Er-rich core and a Zr-rich shell, generally indicated as $Al_3(Er, Zr)$ [9–11]. Zr, in fact, is characterized by a very low diffusion coefficient in Al, as reported in [12], which results in slow coarsening of the abovementioned core-shell dispersoids during high temperature exposure. Furthermore, Zr-rich shell has a kinetically stable $L1_2$ crystal structure and a low lattice mismatch with Al matrix, resulting in enhanced pinning effect for dislocations [9–11].

Thus, the scope of this paper is the characterization of the influences

* Corresponding author.
E-mail addresses: marco1.colombo@polimi.it (M. Colombo), elisabetta.gariboldi@polimi.it (E. Gariboldi), alessandro.morri4@unibo.it (A. Morri).

Published Journal Article available at: https://doi.org/10.1016/j.msea.2017.12.068

Table 1
Chemical composition in wt% of the studied alloys, obtained from GDOES measurements.

	Si	Mg	Fe	Ti	B	Er	Zr	Al
E3	7.38	0.36	0.08	0.14	0.0001	0.22	–	bal
EZ31	7.34	0.38	0.09	0.11	0	0.26	0.14	bal
EZ33	7.37	0.35	0.09	0.11	0	0.26	0.25	bal
EZ35	6.85	0.34	0.09	0.12	0.0003	0.25	0.59	bal

of Zr additions on the microstructure, room and high temperature mechanical properties and overaging resistance of a previously described Er-containing Al-7Si-0.4Mg alloy.

2. Materials and methods

Al-15 wt% Er and Al-10 wt% Zr master alloys were added to a standard Al-7Si-0.4Mg (commercial A356 alloy) to obtain the alloys with the chemical composition reported in Table 1. Zr content was selected in order to have, according to the Al-Zr phase diagram reported in [13], hypo-peritectic, peritectic and hyper-peritectic compositions (named respectively EZ31, EZ33 and EZ35). E3 alloy, which was characterized in [5], is reported as a reference. The low concentration of B in the alloys prevents any grain refinement effect from this ele-ment.

The master and reference alloys were melted in an induction furnace at the casting temperature of 1073 K, under Ar atmosphere. The melt was hold for 30 min at the same temperature and subjected to magnetic stirring, to homogenize its chemical composition. The alloys were then poured in a permanent steel mould, pre-heated to 473 K. The ingots had the shape of cylinders with 40 mm diameter and 120 mm in height.

Samples with $10 \times 10 \times 10$ mm^3 approximate size were extracted from the bottom of the cast bars for microstructural analyses and microhardness tests. Microstructure of the alloys was characterized, in the as-cast and peak aged states, after conventional metallographic polishing and etching with Keller's reagent. Thermal treatment was composed by: 5 h Solution Heat Treatment (SHT) at 813 K, quenching in room temperature water and immediate aging at 473 K.

Optical microscope was used to qualitatively identify the presence of intermetallics and to acquire quantitative microstructural informa-tion such as Secondary Dendrites Arm Spacing (SDAS), morphology of eutectic Si and area fraction of casting defects, by using ImageJ software. SDAS was measured by means of low magnification optical micrographs in the as-cast condition, with at least 100 measurements for each alloy. The morphology of eutectic Si was characterized in the as-cast and peak aged conditions, approximating every Si particle as an ellipse; the major axis, the minor axis and the aspect ratio (defined as the ratio between the major and the minor axis) of each ellipse were measured and used as characterizing parameters. At least 1500 Si particles for each alloy and heat treatment condition were analysed. Finally, the area fraction of pores for the studied alloys was calculated by dividing the total area of defects (measured without any morphological simplification using ImageJ), by the total area of the micrographs. Reported values are the average of the measurements performed on five 25x optical micrographs.

Scanning Electron Microscope (SEM) and Energy Dispersive X-ray Spectrometry (EDS) were used to better describe the morphology, the area fraction and the chemical composition of the intermetallics present in the alloys. To easily obtain morphological information on the intermetallics, micrographs acquired using backscattered electrons (BSE) were analysed. Intermetallics were approximated as ellipses and their major axis, minor axis and aspect ratio were used to characterize their morphology. The area fraction of intermetallics, on the other hand, was calculated dividing the total area of intermetallics (measured without any morphological simplification using ImageJ) by the total area of the micrographs. The reported values are obtained using at least three SEM images at the same magnification, considering a total area of approximately 4,090,000 μm^2 for each alloy.

Vickers microhardness tests were performed with an indenter load of 2.94 N; each reported value is the average of 10 measurements.

Mechanical properties of the studied alloys were obtained by means of tensile tests, performed on specimens extracted from the central part of cast cylinders. The ingots were heat treated following the abovementioned heat treatment and machined in accordance to ASTM E8M-REV A specifications [14], to obtain tensile test specimens with a circular cross section. A gauge length of 30 mm and a gauge diameter of 6 mm were chosen. Tensile tests were performed on the alloys in the T6 temper at 298, 423 and 473 K and in the overaged condition (after 168 h exposure at 473 K) at 298 and 473 K. Tensile tests were per-formed in displacement control mode, with a displacement rate of the crosshead of 0.017 mm/s.

The fracture surfaces of the tensile specimen were analysed by means of optical and SEM microscopes, to characterize fracture mechanisms.

3. Results

3.1. Microstructural characterization

Low magnification micrographs of the studied alloys in the as-cast state are reported in Fig. 1. All the alloys are characterized by α-Al dendrites, eutectic Si and different families of intermetallics. The microstructure of alloy EZ35, reported in Fig. 1d, clearly highlights the globular morphology of dendrites for this alloy.

The results reported in Table 2 show that, even if SDAS values of EZ31 and EZ33 are statistically the same, a clear progressive reduction of SDAS as Zr content is increased can be appreciated. There is, in fact, a reduction of 10.4%, 12.0% and 24.5% in SDAS mean values with respect to E3 for EZ31, EZ33 and EZ35 respectively.

To account for the globular morphology of dendrites in EZ35, SEM micrographs were taken. Fig. 2 reports a representative micrograph of the central region of a dendrite in EZ35; it is characterized by the presence of elongated intermetallics with a complex shape, in close association with smaller particles, some of which are highlighted by arrows in the same figure. EDS analyses were performed on one of the abovementioned small particles (point A in Fig. 2) and, even though its small size prevents from precise information about its chemical composition, an enrichment in Er with respect to the bigger intermetallic (point B in Fig. 2) can be observed.

To characterize the morphology of eutectic Si in the as-cast state, high magnification optical micrographs were taken, and are reported in Fig. 3. Quantitative analysis results, summarized in Table 3, suggest that the aspect ratio of Si is approximately constant for all the alloys, with a value ranging from 1.5 to 1.7. On the other hand, they reveal that Zr addition reduces the eutectic major axis: for E3 it has an average value of 3.5 μm, while for Zr-containing alloys it is around 2.4 μm.

When dealing with innovative Al alloys based on the Al-Si-Mg system, it is very important to consider the presence of pores, since even a low amount of these casting defects can affect the ductility and UTS of the alloy [15,16]. For this reason, percent area fraction of these defects was measured for the alloys under investigation. The results of this analysis are reported in Table 4 and do not highlight significant effects of Zr on porosity.

The high temperature exposure during SHT causes a slight reduction in the eutectic Si aspect ratio, while the average major axis increases with respect to the as cast condition, as shown in Table 5.

After SHT, several intermetallics are observed in the alloys, as reported in Fig. 4.

As described in [5], E3 is characterized by different families of Er-containing intermetallics: elongated precipitates with an average length of about 20 μm (A in Fig. 4a), blocky shaped and small globular

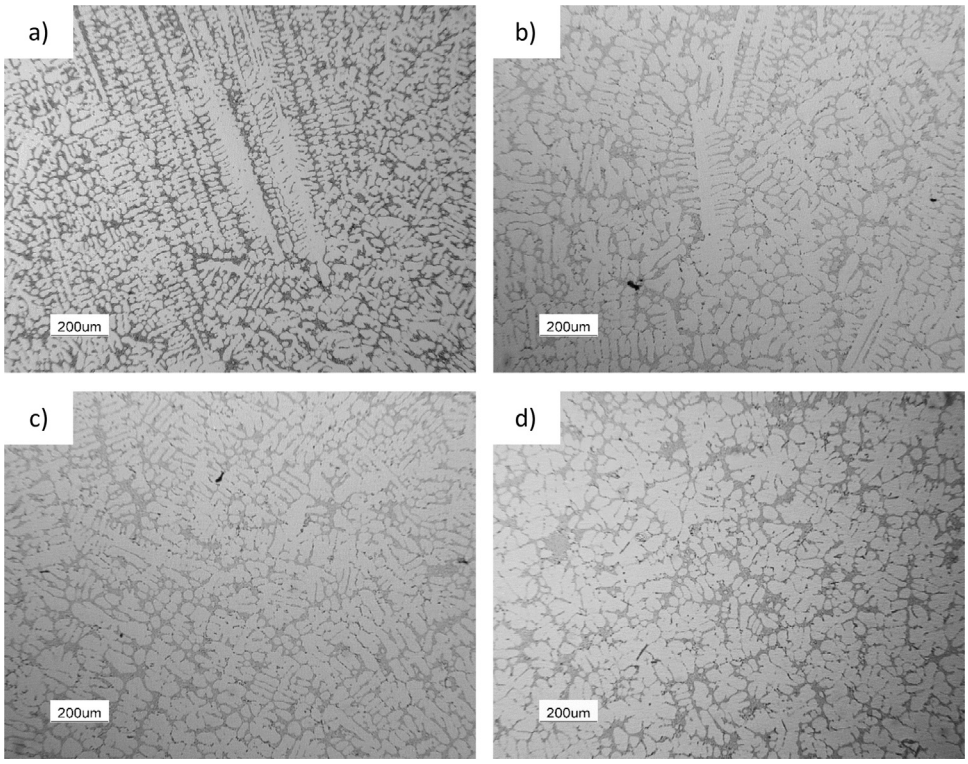

Fig. 1. Low magnification micrographs of a) E3, b) EZ31, c) EZ33 and d) EZ35 in the as-cast state.

Table 2
Measured SDAS for E3 and EZ31, EZ33 and EZ35 alloys.

	Measured SDAS (μm)
E3	24.1 ± 0.9
EZ31	21.6 ± 1.5
EZ33	21.2 ± 1.4
EZ35	18.2 ± 1.1

intermetallics (respectively B and C in Fig. 4a).

Zr-containing alloys are characterized by additional intermetallics enriched in Zr. Specifically, in EZ31 are visible intermetallics containing Zr and Er (D in Fig. 4b), in close association with precipitates containing Mg, Fe and Er (E in Fig. 4b) and small intermetallics enriched in Er and Fe (F in Fig. 4b). EZ33 is additionally characterized by a low amount of complex shaped intermetallics, as shown in Fig. 4c, enriched in Zr and Er (G in Fig. 4c) and Zr, Ti and Er (H in Fig. 4d). Finally, EZ35 has small intermetallics containing Mg and Er (I in Fig. 4d) and precipitates containing Fe, Mg and Er, with a chemical composition similar to particle E (L in Fig. 4d). Further, as shown in Fig. 2, intermetallics enriched in Si, Zr and Ti are present in the central region of the dendrites of this alloy.

Table 6 lists the results of quantitative analyses carried out on the morphology of the intermetallics present in the alloys, comparing their as-cast and SHT state: average area fraction, average aspect ratio and major axis are reported. In the as-cast state, E3 is characterized by a lower amount of intermetallics, which also show lower average major axis with respect to those in Zr-containing alloys. No significant difference, on the other hand, is found in their average aspect ratio. The highest amount of intermetallics is found in EZ31. Intermetallics in the central region of the dendrites (which occupy a total area fraction of 0.19%) are included in the value given in Table 6 for EZ35.

After SHT, the average major axis of the intermetallics slightly reduces with respect to the as-cast condition in all the investigated alloys, possibly due to partial dissolution induced by high temperature exposure during SHT. The area fraction of intermetallics decreases after SHT for E3, EZ31 and EZ33, while it remained almost constant for EZ35. As far as the aspect ratio is concerned, SHT does not induce significant modifications.

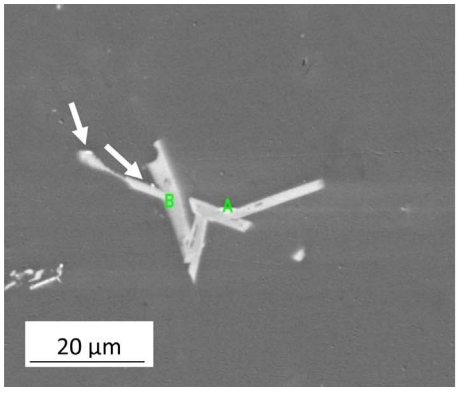

	at% Al	at% Si	at% Ti	at% Zr	at% Er
A	67.21	14.56	2.87	9.08	6.28
B	63.22	14.20	10.21	12.31	0.05

Fig. 2. SEM micrograph of EZ35 showing intermetallics in the central region of the dendrite; results of EDS analysis on the intermetallics are also reported. Er-containing intermetallics are highlighted by arrows and in measurement point A.

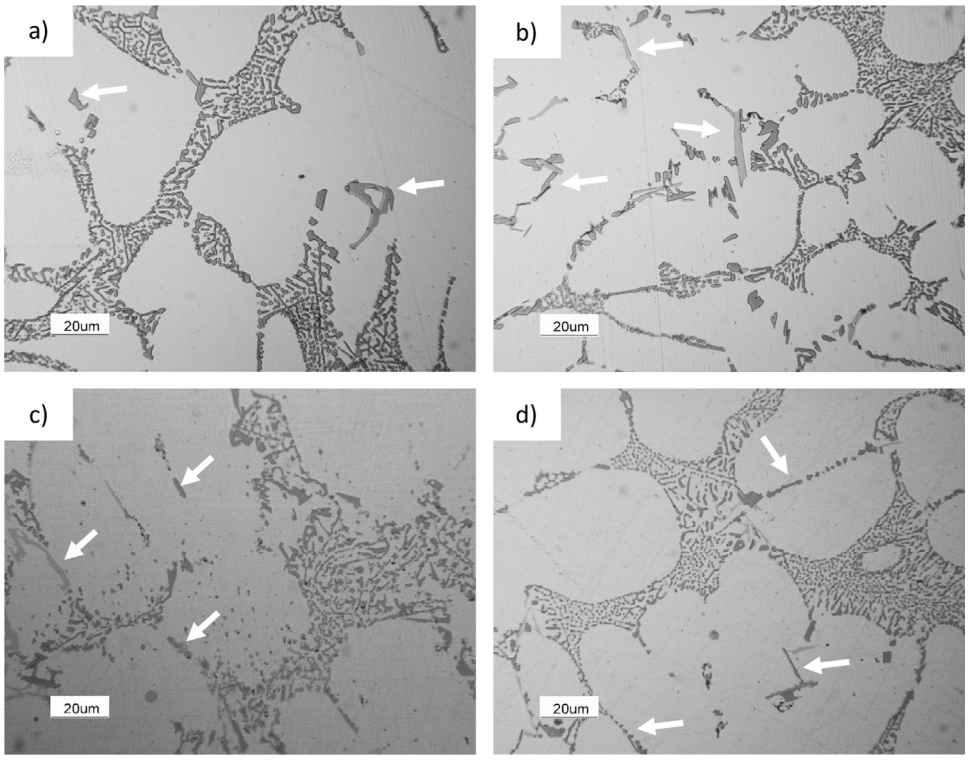

Fig. 3. High magnification micrographs of a) E3, b) EZ31, c) EZ33 and d) EZ35 in the as-cast state showing the eutectic morphology. Intermetallics are highlighted by arrows.

Table 3
Aspect of eutectic Si in EZ31, EZ33 and EZ35 in the as-cast state.

	E3	EZ31	EZ33	EZ35
Aspect ratio	1.6 ± 0.5	1.5 ± 0.2	1.7 ± 0.4	1.7 ± 0.3
Average major axis (μm)	3.5 ± 0.6	2.4 ± 0.8	2.4 ± 0.7	2.3 ± 0.6

Table 4
Percent area fraction of defects for the studied alloys.

	E3	EZ31	EZ33	EZ35
Area fraction of defects	1.11% ± 0.31	1.14% ± 0.32	1.14% ± 0.28	1.17% ± 0.15

Table 5
Aspect of eutectic Si in EZ31, EZ33 and EZ35 after SHT.

	E3	EZ31	EZ33	EZ35
Aspect ratio	1.2 ± 0.2	1.3 ± 0.3	1.3 ± 0.2	1.3 ± 0.3
Average major axis (μm)	4.5 ± 0.7	4.5 ± 0.8	4.6 ± 0.7	4.5 ± 0.6

3.2. Mechanical properties

The response to aging of EZ alloys is shown in Fig. 5 in terms of Vickers hardness as a function of the logarithm of the aging time. The aging curve of alloy E3 is added for comparison.

The microhardness of the alloys before the starting of aging, which ranges between 60 and 65 HV, increases as a function of Zr concentration, as well as their peak hardness, with a minimum value of 108.9 HV for E3 and a maximum of 132.8 HV for EZ35. EZ31 and EZ33 are characterized by 109.6 HV and 114 HV peak hardness, respectively. EZ35 shows also a faster hardening kinetic, reaching the peak hardness in 1.5 h, while all the other alloys reached the T6 temper after 3 h. It can be observed that, after 168 h aging, the residual microhardness of Zr-containing alloys is higher than for E3, with a value that increases as a function of Zr concentration. In fact, an increase of 7.1%, 11% and 14.2% in residual hardness for EZ31, EZ33 and EZ35 respectively was observed with respect to E3 (71.1 HV).

The results of tensile tests performed on EZ alloys are reported in Fig. 6 for the peak aged condition; results of the tests performed on E3 and described in [5] are reported as a reference. They clearly show that the addition of Zr is beneficial for the mechanical properties of the alloys. In particular, EZ35 shows the maximum YS, UTS and e% in all the testing conditions. Considering E3 as a reference, the increase of YS, UTS and e % for EZ35 is 7.9%, 3.8% and 8.9% at room temperature, 11.3%, 14.8% and 2.0% at 423 K and 14.2%, 18.7% and 14.5% at 473 K, respectively.

The results of tensile tests performed after 168 h overaging are reported in Fig. 7. As in the peak aged condition, the addition of Zr to E3 increased the mechanical properties of the alloy. Also in this case, EZ35 showed the highest mechanical properties. Comparing the results obtained from EZ35 with the ones from E3, the increase of YS, UTS and e % is 15.0%, 8.5% and 28.6% at room temperature and 18.5%, 21.0% and 33.1% at 473 K.

3.3. Fractographic analyses

Fracture surfaces of the studied alloys tested at room temperature in the peak aged condition, reported in Fig. 8, enable to describe the general failure mechanisms of the studied alloys. The low ductility emerged from tensile tests on EZ31 and EZ33 alloys can be explained considering the presence of a high amount of complex-shaped intermetallics in proximity of the fracture surfaces, as shown by the SEM micrographs reported in Fig. 9.

4. Discussions

4.1. Microstructural characterization

The development of the as cast microstructure of the alloys is influenced by nucleation and growth of dendrites, which are ultimately affected by the Zr content in the alloys. The effects of Zr on nucleation

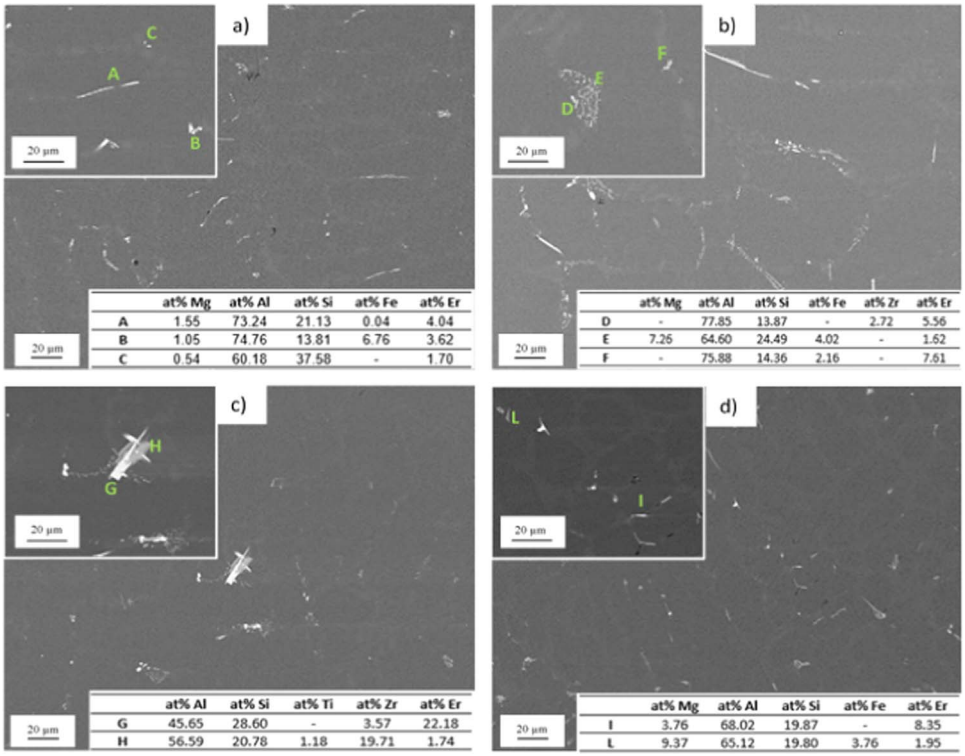

Fig. 4. Intermetallics present in a) E3, b) EZ31, c) EZ33 and d) EZ35 after SHT. Insets show characteristics intermetallics, on which EDS analyses where performed. The results of the analyses are reported in the micrograph of the correspondent alloy.

Table 6
Average area fraction, major axis and aspect ratio for the intermetallics derived from metallographic analyses of the investigated alloys in their as-cast condition and after SHT. The values for the major axis are given in μm.

	As cast			After SHT		
	Area fraction	**Average major axis**	**Average aspect ratio**	**Area fraction**	**Average major axis**	**Average aspect ratio**
E3	0.90% ± 0.09	7.16 ± 2.10	2.91 ± 0.65	0.49% ± 0.10	6.14 ± 1.96	2.34 ± 0.81
EZ31	1.46% ± 0.13	10.59 ± 3.01	2.93 ± 1.30	1.38% ± 0.20	9.85 ± 2.58	2.91 ± 1.03
EZ33	1.13% ± 0.10	9.99 ± 2.65	2.64 ± 1.08	0.90% ± 0.09	8.85 ± 2.11	2.39 ± 0.96
EZ35	0.96% ± 0.14	9.77 ± 2.87	2.76 ± 1.01	1.08% ± 0.07	8.43 ± 2.02	2.87 ± 1.05

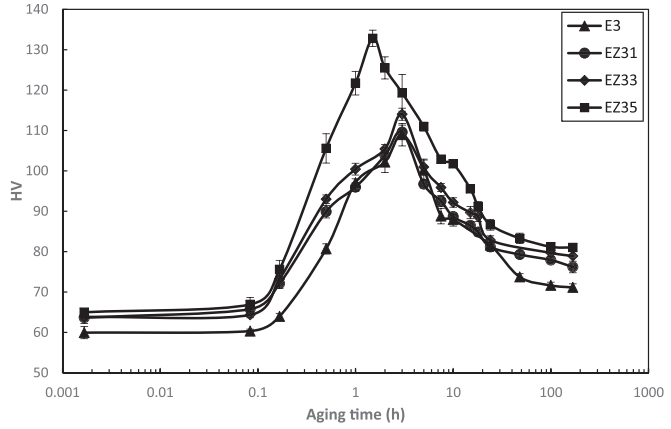

Fig. 5. Microhardness evolution of E3 and of EZ series during aging at 473 K.

and growth of Al dendrites will be hereafter described separately.

A classical cast microstructure with dendrites elongated along the direction of heat flux can be observed in Zr-free and low-Zr alloys, while EZ35 is characterized by dendrites with globular shape, as it is visible from Fig. 1d. The reported differences could be explained con-sidering the Al-Zr binary phase diagram [13]: when Zr is added with a concentration of 0.59 wt%, pro-peritectic Zr-containing intermetallics are present in the melt, acting as inoculants for α-Al dendrites [17]. The SEM micrograph reported in Fig. 2 confirms the theoretical analysis of the phase diagram, highlighting the presence of elongated inter-metallics in the central region of EZ35 dendrites. Comparing their EDS analyses with literature data, they can be identified as $(Al, Si)_3(Zr, Ti)$, for which wide compositional ranges are proposed in literature [4,18,19]. Since the concentration of Ti in the alloys is only slightly beyond its maximum solubility in Al at the peritectic temperature (which is reported to be around 0.1 wt% in [20]), it is reasonable that this family of particles derives from $(Al, Si)_3Zr$, rather than from $(Al, Si)_3Ti$, and experienced a partial substitution of Zr by Ti atoms. Further, as reported in literature, the relatively low concentration of Si in the alloy is not sufficient to promote the precipitation of $(Si, Al)_2Zr$ [21].

It is known from literature that inoculation is ruled by group symmetry of inoculant and its lattice mismatch with the inoculated species. Even if no group symmetry nor lattice parameter information were found in literature for $(Al, Si)_3(Zr, Ti)$, it is reported that $Al_3(Zr, Ti)$ has a metastable $L1_2$ group symmetry (the same of α-Al) and a very low lattice mismatch with the matrix (below 1% at room temperature [22]), making it a powerful nucleation agent for Al dendrites [23,24]. It can be suggested that the presence of Si in the abovementioned inter-metallics would not induce drastic changes in the inoculation efficacy of $(Al, Si)_3(Zr, Ti)$, but further studies are needed to clarify this aspect.

$(Al, Si)_3(Zr, Ti)$ intermetallics were frequently found in association with Er-containing small particles during microscopic investigations, as

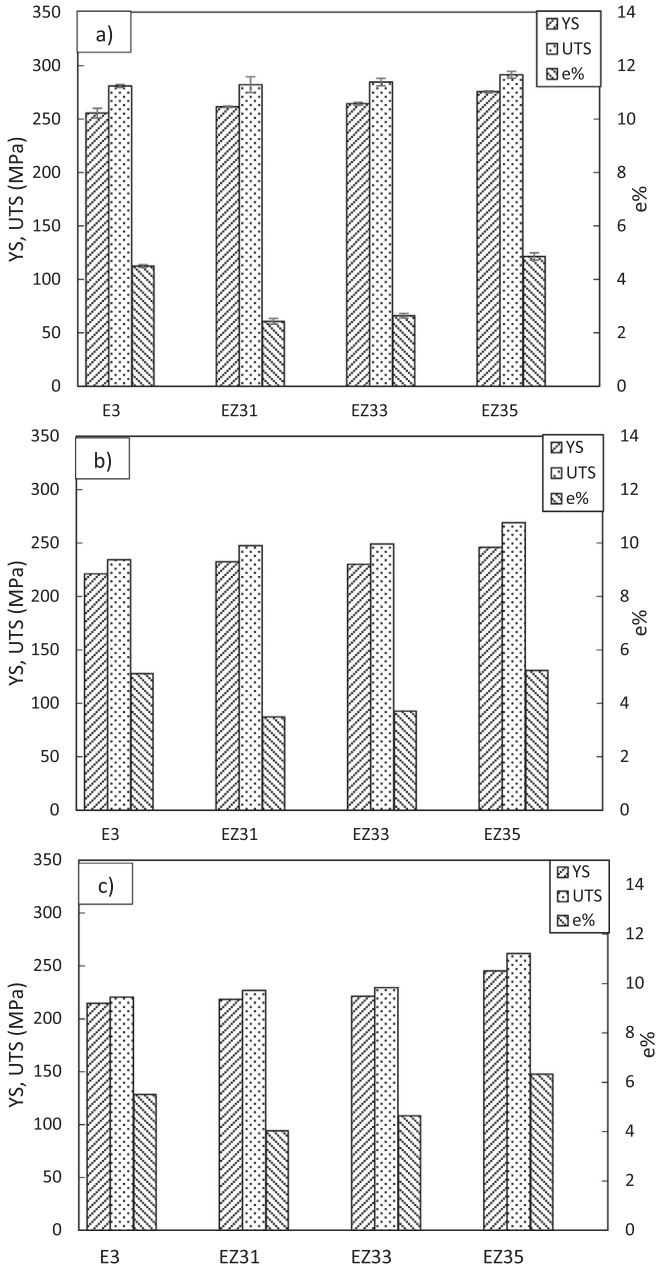

Fig. 6. Results of the tensile tests performed on EZ series at a) 298, b) 423 and c) 473 K in the peak aged condition. Results of tensile tests performed on E3 are reported as a reference.

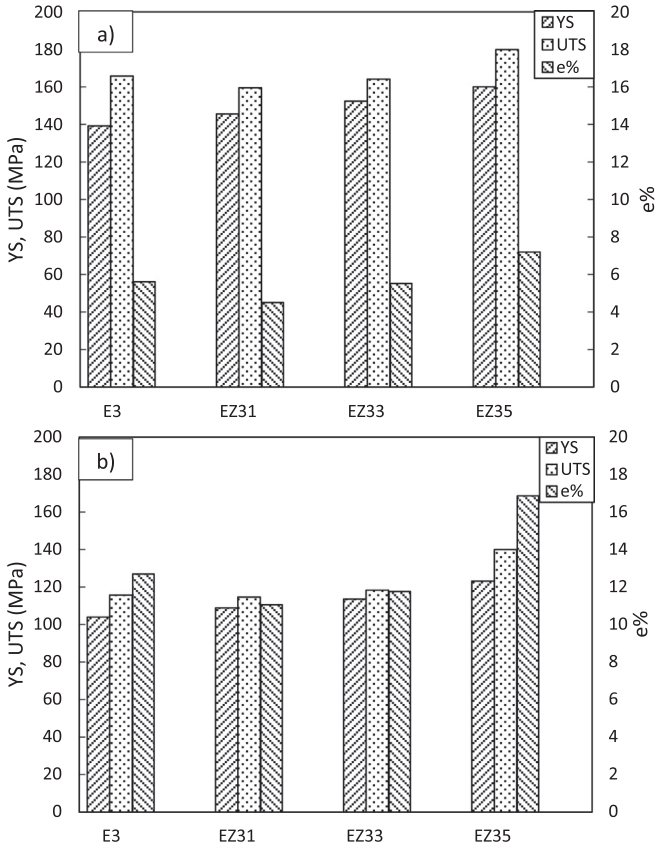

Fig. 7. Results of the tensile tests performed on EZ series at a) 298 and b) 473 K after 168 h at 473 K.

it is shown in Fig. 2 and in the relative EDS analysis. A heterogeneous nucleation of Er-containing intermetallics on $(Al, Si)_3(Zr, Ti)$ can also be suggested, since they are always found at the interface between $(Al, Si)_3(Zr, Ti)$ and α-Al, as highlighted in the representative micrograph in Fig. 2.

The absence of $(Al, Si)_3(Zr, Ti)$ intermetallics in EZ31 and EZ33 and the concomitant elongated morphology of Al dendrites in the microstructure of these alloys further confirm the role of $(Al, Si)_3(Zr, Ti)$ intermetallics for effective dendritic inoculation. Zr concentrations lower than the peritectic value, in fact, are found to have negligible effects on dendrites nucleation.

SDAS is used as a parameter to characterize the influence of Zr on dendritic growth. SDAS values for the studied alloys are summarized in Table 2 and show a monotonic decrease as the concentration of Zr in alloys increases. It is well known that SDAS is affected by chemical composition of the alloy and by cooling rate during solidification [25].

Since the casting parameters were the same for all the alloys and the differences in chemical composition are too low to induce changes in the thermophysic properties of the melt, it can be concluded that Zr additions are the responsible of SDAS reduction.

The effect of Zr on SDAS reduction and, consequently, on dendritic growth, can be explained using the growth rate restriction approach. Growth rate restriction of dendrites during solidification could be described by the parameter Q, called growth restriction factor. As reported in literature, Q can be thought as a qualitative index to estimate how fast the liquid ahead of the solidification front becomes constitutionally undercooled in the earliest stages of crystals growth [26,27], and can thus be used as a criterion for the microstructural refinement of α-Al dendrites. Literature studies, in fact, report that Q is inversely proportional to the growth rate of α-Al crystals [26,27].

In the case of multicomponent alloys, the use of growth restriction parameter could be critical, especially in the case of strong solute-solute interactions. Nevertheless, literature studies demonstrated that, for dilute alloys, the actual growth restriction factor could be estimated by summing the contribution of each solute independently, without interaction terms [26]. Thus, the effect of Zr can be studied independently from that of other elements.

For Zr, Q can be expressed by Eq. (1), for a wide range of compositions [26]:

$$Q = aC_0 + bC_0^2 \quad (1)$$

Where a = 7.57 K/wt% and b = 9.1 K/wt%^{2} are empirical constant [26], evaluated for hypo-peritectic alloys, while C_0 is the initial concentration of Zr in the alloy. The application of Eq. (1) to the alloys under investigation leads to the results reported in Fig. 10, which shows the comparative trends of Q and SDAS as a function of Zr content in the alloy.

The growth rate restriction parameter clearly increases with the

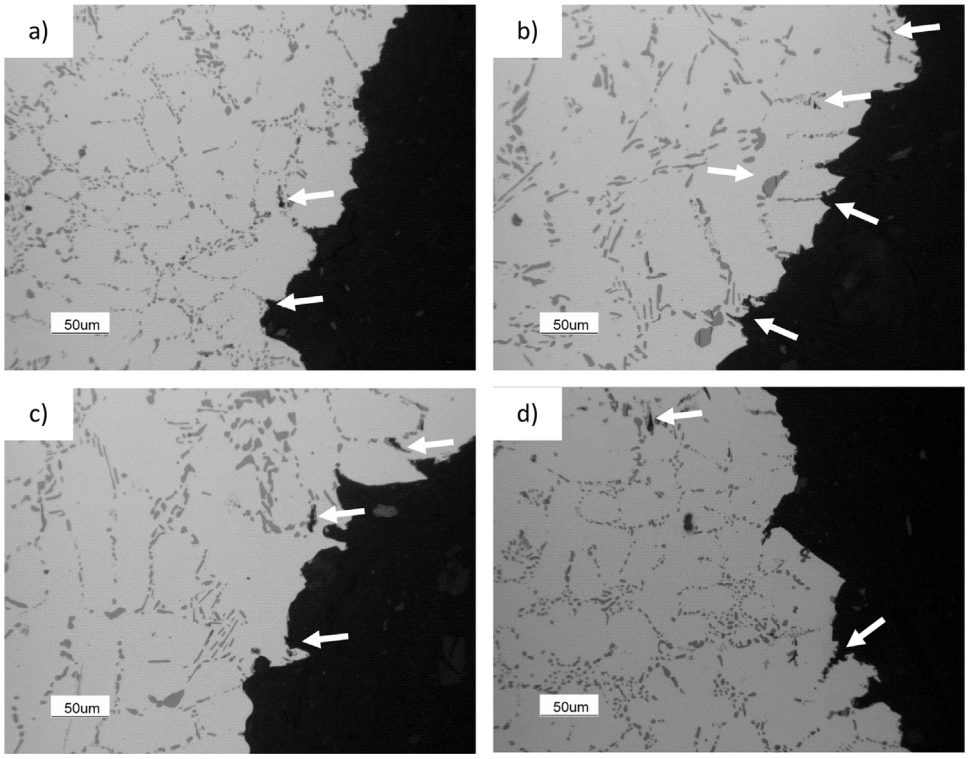

Fig. 8. Fracture surfaces of a) E3, b) EZ31, c) EZ33 and d) EZ35 tested at room temperature in the peak aged condition. Arrows highlight secondary cracks, fractured and debonded particles.

amount of Zr, resulting in a finer microstructure for high-Zr alloys, as confirmed by the lower SDAS values. Zr accumulation ahead of the solidifying dendrites, in fact, is responsible of constitutional undercooling at the dendrites tip, retarding the dendritic growth.

An additional contribution to the refined microstructure of EZ35 could come from the relatively high amount of $(Al, Si)_3(Zr, Ti)$ properitectic intermetallics that, as it was stated before, act as heterogeneous nucleation points for the Al dendrites.

The results of the analyses on eutectic Si geometry, qualitatively seen in Fig. 3 and listed in Table 3, reveal that Zr has not an evident effect on Si aspect ratio, since its value is maintained almost constant in all the alloys. As far as the eutectic size is concerned, there is a sig-nificant reduction in the average major axis of Si when Zr is added, which is not found to be dependent on Zr concentration. This fact can be possibly explained considering the presence of Zr in the eutectic li-quid, which depressed the nucleation temperature of eutectic Si,

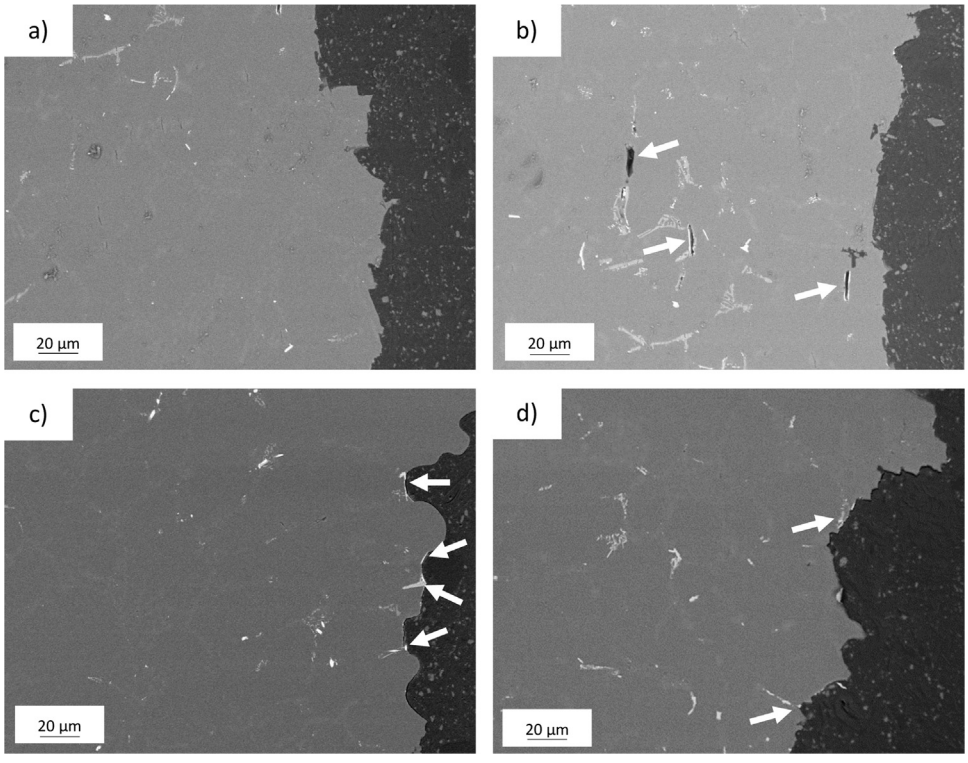

Fig. 9. Representative SEM BSE micrographs of a) E3, b) EZ31, c) EZ33 and d) EZ35 fracture surfaces for samples tested at room temperature in the peak aged condition. Intermetallics on or in the vicinity of the fracture surfaces are highlighted by arrows.

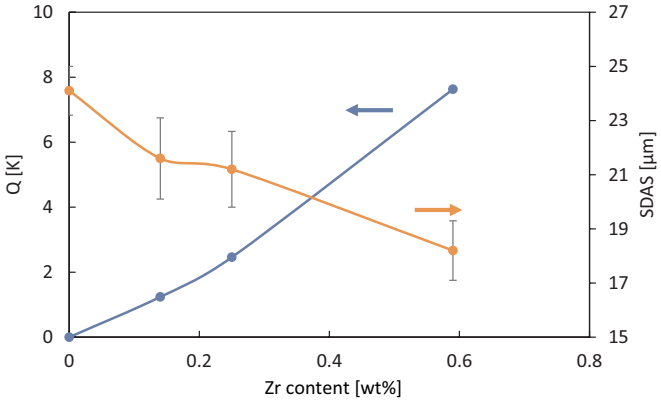

Fig. 10. Graph reporting Q and SDAS as a function of the Zr content in the alloy.

reducing its size. Indirect support of this hypothesis comes from the presence of Zr-containing intermetallics in the eutectic region, as shown in Fig. 4.

Experimental measurements of the percent area fraction occupied by casting defects show that Zr additions do not induce a significant increase in the amount of micro and macro porosities, even for EZ35. Thus, the castability of the alloy seems not to be affected by Zr additions. It was shown in literature that porosity affects strongly the mechanical properties of cast Al-Si-Mg-based alloys [15,16,28–30]; the presence of a similar amount of these casting defects in the investigated materials allows to perform meaningful comparisons of the results extracted from tensile tests.

During high temperature exposure, eutectic Si firstly decomposes to a sphere-like morphology, due to Rayleigh instability, and then coarsens, increasing its size [31]; the whole process is driven by a minimization of the total surface and of the related surface energy of Si. The occurrence of the two phenomena during SHT is confirmed by the increase of the average Si major axis and the reduction in its aspect ratio, which are reported for all the investigated alloys in Table 5 and in Fig. 3.

Fig. 4 reports the results of semi-quantitative analyses on the intermetallics on the SHT alloys; the precise phase identification is made complex by the high number of alloying elements and by the absence in literature of complete phase diagrams for the investigated alloys. Empirical formulas for the analysed intermetallics are reported or proposed in Table 7.

According to the isothermal section of the Al-Si-Er phase diagram made available by Raghavan in [32], alloy E3 should be in the Al + Si + τ_2 ($Er_2Al_3Si_2$) region, but the presence of other alloying elements and the absence of complete phase diagrams prevent more accurate descriptions. In alloys containing Zr, phases identification is even more complicated. Despite the complete lack of literature describing the phases in such complex alloys, some considerations can be made, using simpler systems as references. Intermetallics E and L, for example, show a chemical composition similar to π $Al_8Mg_3Si_6Fe$ phase, typical of Al-Si-Mg alloys, with enrichment in Er. Further, precipitate G has a chemical composition matching that of τ_2 $Er_2Al_3Si_2$ intermetallics, with enrichment in Zr.

SEM micrographs highlight the appearance of rosettae in the alloys microstructure (visible in the inset of Fig. 4(b). This morphology is recognized from its convex and smooth shape and from the presence of fine, multi-phase intermetallics, as reported in Table 7 and in the inset of Fig. 4(b). Some authors proposed that they originate from isolated liquid drops entrapped within the dendritic structure [33,34]. If, as it can be reasonably expected, rosettae form according to the proposed mechanism, it can be assumed that nucleation of the intermetallics inside them is heterogeneous, and starts at the interface with the surrounding α-Al. The high undercooling needed to trigger nucleation of intermetallics inside the entrapped liquid could explain their very fine size in the rosettae. This hypothesis was confirmed in other literature works, in which similar structures were found [33,34].

The calculated area fraction of intermetallics reported in Table 6 for the different alloys highlights their relatively low amount in EZ35 alloy. Since the intermetallics present in the alloys are rich in Si (as described in the EDS analyses reported in Fig. 4), it is reasonable to presume that the reduced Si content in EZ35, emerged from GDOES analyses reported in Table 1, may have affected their number and dimensions. Comparisons of the area fraction values reported in Table 6 further shows the greater tendency of intermetallics in alloy E3 to dissolve during SHT; this could be due to their smaller size with respect to the intermetallics in EZ alloys, but also to the higher diffusion coefficient of Er with respect to Zr at this temperature in Al. Diffusivity of Er and Zr, in fact, are calculated to be 4.71×10^{-17} m^2/s and 2.06×10^{-17} m^2/s respectively, using the pre-exponential term and activation energy reported in literature [8,12]. The low diffusivity of Zr at the SHT temperature (optimized for A356 alloy) could explain the only slight response of Zr-containing coarse intermetallics to this heat treatment.

4.2. Mechanical properties and fracture surfaces

The aging curves of the studied alloys are reported in Fig. 5. The higher concentration of alloying elements in the α-Al dendrites possibly translates into a shorter time needed for the formation of strengthening dispersoids and could explain the faster aging kinetics observed for the alloy.

The peak hardness of the studied alloys is found to increase as a function of Zr concentration, possibly due to the increase in the number of Er- and Zr-containing strengthening dispersoids (Al_3(Er, Zr)), as it was demonstrated in studies on pure Al microalloyed with Er and Zr [10,35,36]. Other contributions to the increased microhardness of EZ35 could come from the presence of pro-peritectic Zr-rich intermetallics and from the refined microstructure. The region of the curves corre-sponding to prolonged overaging highlights that the microstructural stability of the studied alloys increases as a function of Zr content. This could be considered, as proposed in literature [36], an indirect proof of the formation of the abovementioned Er- and Zr-containing nanometric precipitates with enhanced coarsening resistance and retarded coherency loss. Their enhanced coarsening resistance is caused by the very low diffusion coefficient of Zr in Al, which retards Ostwald ripening. On the other hand, the reduced lattice parameter mismatch of Zr-containing precipitates with Al (lower than 1% at room temperature) explains the retarded coherency loss of the precipitates [36,37]. Further microstructural analyses (e.g. TEM or Atom Probe Tomography) are, however, needed to confirm the presence of the strengthening particles mentioned before and their role in increasing the mechanical properties of the studied alloys.

As regards the outcome of tensile tests, Figs. 6 and 7 report an increase in the mechanical strength as a function of Zr concentration in

Table 7
Most relevant intermetallics in the studied alloys (letters identifying the intermetallics refer to Fig. 4) with the actual empirical formula.

Alloy	Intermetallic	Empirical formula
E3	A	$Al_{18}Si_5Er$[a]
	B	$Al_{20}Si_4Fe_2Er$[a]
	C	$Al_{35}Si_{22}Er$[a]
EZ31	D	Al_9Si_2(Er, Zr)
	E	Al_{16}(Mg, Er)$_3Si_6Fe$[a]
	F	$Al_{35}Si_7Er_3Fe$[a]
EZ33	G	Al_3Si_2(Er, Zr)$_2$
	H	Al_3Si(Zr, Er)
EZ35	I	Al_6Si_2(Er, Mg)
	L	Al_{17}(Mg, Er)$_3Si_5Fe$[a]

[a] Due to the small sizes of the intermetallics and to their position in interdendritic region, high Si and/or Al content are due to the contribution of the surrounding eutectic.

Table 8
Quality indices of the studied alloys at different testing temperatures and aging conditions.

	Peak aged			Overaged	
	298 K	**423 K**	**473 K**	**298 K**	**473 K**
E3	378.9	340.7	331.7	278.1	281.2
EZ31	339.9	328.9	317.7	257.7	271.1
EZ33	347.8	334.5	329.5	275.5	278.9
EZ35	394.4	376.8	382.1	319.3	324.0

the alloys for all the tested conditions. Results reported in Figs. 6b, 6c, 7a and 7b show that, as the testing temperature and aging time increase, the YS and UTS of Zr-containing alloys, and especially of EZ35, remain higher than those of E3. This is a clear indication of the improved high temperature resistance and microstructural stability of the Zr-containing alloys with respect to E3. This experimental evidence is an indirect confirmation of the presence of strengthening precipitates, which have slow coarsening rates and are very effective in pinning dislocations. As for the alloys ductility, there is not a unique trend: after an initial drop for 0.1 wt% Zr addition, e% increases monotonically for the other two alloys, with EZ35 that shows, in all conditions, the highest elongation to fracture. It is known from scientific literature that the ductility of Al-Si cast alloys is significantly influenced by the amount of porosity, the morphology of eutectic Si and by the number and morphology of intermetallics [5,15,16,38]. Since the amount of porosity is almost constant in all the alloys and eutectic Si is well modified, the most relevant parameters affecting the alloys' ductility are the amount of intermetallics, their size and their morphology. The high area fraction and large sizes of intermetallics of EZ31, reported in Table 6, could therefore explain its reduced ductility.

Despite EZ35 is characterized by similar amount and size of intermetallics with respect to EZ33 (as reported in Table 6), its ductility is the highest among the investigated alloys. To explain this apparent incongruence, it should be considered that a fraction of intermetallics is in the central region of the dendrites, as shown in Fig. 2, so that their stress intensification action is supposed to be mitigated by the ductility of the surrounding matrix. Further, the increased ductility could come from the lower Si content in the chemical composition of the alloy, reported in Table 1. It is well known that fracture in cast Al-Si alloys can develop from delaminated or cracked eutectic Si particles. A lower Si concentration could, therefore, reduce the number of potential nucleation sites for cracking, thus contributing to increase the alloy's ductility.

The quality index approach is proposed to better characterize the effects of Zr additions on the mechanical properties of the studied alloys [39]. Since this index includes UTS and e%, it is a good indicator of the mechanical performances of the studied alloys. The quality index, in its original formulation, is described in [39] and reported in Eq. (2):

$$QI = UTS + k\log(e\%) \quad (2)$$

Where QI is the quality index and k is a constant, equal to 150 MPa for A356 [40].

UTS and e% are strongly affected by porosity in Al-Si-based alloys, as reported in literature [5,15,16] and mentioned above, so that the use of quality index could lead to results dependent not only on the ma-terial, but also on the presence of defects. Since for all the studied alloys the Si amount is within the range of composition prescribed by the standards for commercial A356 [41] and the percent area fraction of pores is similar, QI can be considered a meaningful parameter to evaluate the effects of Zr additions on the mechanical properties of E3 alloy.

Quality indices for the studied alloys, tested at different temperatures and different aging conditions, are reported in Table 8.

At a fixed temper condition and test temperature, QI reflects the results of tensile test: an initial reduction for EZ31 and then a monotonic increase, with a maximum value for EZ35 in all the tested conditions. This evidence confirms that EZ35 is characterized by the highest mechanical strength and ductility among the studied alloys.

Analyses of fracture surfaces reported in Fig. 8 confirm the general fracture mechanisms proposed in literature for Al-Si cast alloys [38]. Primary cracks develop in the eutectic region: debonded and cracked Si particles can be observed close to the fracture surfaces, as highlighted by arrows in Fig. 8. The BSE micrographs in Fig. 9 show the presence of complex shaped intermetallics in the eutectic region at or close the fracture surface, especially in EZ31 and EZ33 (Figs. 9b and 9c, respectively). This evidence is a confirmation of the importance of the presence of intermetallics, especially in interdendritic regions, in influencing the ductility of the two alloys.

5. Conclusions

The present work was aimed at identifying innovative Al alloys characterized by improved mechanical properties at room and elevated temperatures and good ductility, to extend the applicability of Al-Si-Mg alloys. From the analyses of the obtained results it emerged that:

- Additions of Zr cause a reduction of SDAS, connected to solute enrichment at the dendrite-liquid interface that restricts the dendrites growth rate and to the presence of pro-peritectic intermetallics,
- The nominal addition of 0.6 wt% of Zr causes a globular dendritic microstructure, due to the precipitation of pro-peritectic $(Al, Si)_3(Ti, Zr)$ intermetallics that act as effective inoculants for α-Al dendrites. This, coupled with growth rate restriction due to solute enrichment at the interface, explains the drastic microstructural refinement seen for EZ35,
- The additions of Zr have a positive influence on the mechanical properties of the alloys, both in the peak aged and overaged condition. Microhardness monotonically increases as a function of Zr concentration, similarly to YS and UTS in all the tested conditions. Ductility, on the other hand, decreases for low Zr concentrations, while for EZ35 it strongly increases. Ductility loss for EZ31 and EZ33 is possibly due to the high amounts of intermetallics present in the interdendritic region; marked ductility increase for EZ35 is due to the globular nature of the dendrites, combined with a less critical distribution of intermetallics in the alloy microstructure and a lower amount of Si in the alloy's composition,
- Quality index is maximum for EZ35 in all the temper conditions and testing temperatures, indicating high strength and ductility for this alloy.

References

[1] K.E. Knipling, D.C. Dunand, D.N. Seidman, Criteria for developing castable, creep-resistant aluminum-based alloys – a review, Z. Met. 97 (2006) 246–265.
[2] S.K. Shaha, F. Czerwinski, W. Kasprzak, J. Friedman, D.L. Chen, Ageing characteristics and high-temperature tensile properties of Al–Si–Cu–Mg alloys with micro-additions of Cr, Ti, V and Zr, Mater. Sci. Eng. A 652 (2016) 353–364.
[3] S.K. Shaha, F. Czerwinski, W. Kasprzak, J. Friedman, D.L. Chen, Effect of Zr, V and Ti on hot compression behavior of the Al–Si cast alloy for powertrain applications, J. Alloy. Compd. 615 (2014) 1019–1031.
[4] J. Hernandez-Sandoval, G.H. Garza-Elizondo, A.M. Samuel, S. Valtierra, F.H. Samuel, The ambient and high temperature deformation behaviour of Al–Si–Cu–Mg alloy with minor Ti, Zr, Ni additions, Mater. Des. 58 (2014) 89–101.
[5] M. Colombo, E. Gariboldi, A. Morri, Er addition to Al-Si-Mg-based casting alloy: effects on microstructure, room and high temperature mechanical properties, J. Alloy. Compd. 708 (2017) 1234–1244.
[6] Z.M. Shi, Q. Wang, G. Zhao, R.Y. Zhang, Effects of erbium modification on the microstructure and mechanical properties of A356 aluminum alloys, Mater. Sci. Eng. A 626 (2015) 102–107.
[7] X. Chen, Z. Liu, S. Bai, Y. Li, L. Lin, Alloying behavior of erbium in an Al-Cu-Mg alloy, J. Alloy. Compd. 505 (2010) 201–205.
[8] Y. Zhang, K. Gao, S. Wen, H. Huang, Z. Nie, D. Zhou, The study on the coarsening process and precipitation strengthening of Al_3Er precipitate in Al–Er binary alloy, J. Alloy. Compd. 610 (2014) 27–34.
[9] H. Li, Z. Gao, H. Yin, H. Jiang, X. Sua, J. Bin, Effects of Er and Zr additions on

precipitation and recrystallization of pure aluminium, Scr. Mater. 68 (2013) 59–62.
[10] Z. Gao, H. Li, Y. Lai, Y. Ou, D. Li, Effects of minor Zr and Er on microstructure and mechanical properties of pure aluminium, Mater. Sci. Eng. A 580 (2013) 92–98.
[11] S.P. Wen, K.Y. Gao, Y. Li, H. Huang, Z. Nie, Synergetic effect of Er and Zr on the precipitation hardening of Al–Er–Zr alloy, Scr. Mater. 65 (2011) 592–595.
[12] K. Hirano, S. Fujikawa, Impurity diffusion in aluminum, J. Nucl. Mater. 69 (1978) 564–566.
[13] H. Okamoto, Al-Zr (Aluminum-Zirconium), J. Phase Equilibria 14 (1993) 455.
[14] Standard Test Methods for Tension Testing of Metallic Materials, ASTM standard, 2016.
[15] C.D. Lee, Effects of microporosity on tensile properties of A356 aluminum alloy, Mater. Sci. Eng. A 464 (2007) 249–254.
[16] C.H. Càceres, On the effect of macroporosity on the tensile properties of the Al-7% Si-0.4%Mg casting alloy, Scr. Metall. Mater. 32 (1995) 1851–1856.
[17] Feng Wang, Z. Liu, D. Qiu, J.A. Taylor, M.A. Easton, M. Zhang, Revisiting the role of peritectics in grain refinement of Al alloys, Acta Mater. 61 (2013) 360–370.
[18] W. Kasprzak, B.S. Amirkhiz, M. Niewczas, Structure and properties of cast Al–Si based alloy with Zr–V–Ti additions and its evaluation of high temperature performance, J. Alloy. Compd. 595 (2014) 67–79.
[19] A.M.A. Mohamed, F.H. Samuel, S. Alkahtani, Microstructure, tensile properties and fracture behavior of high temperature Al–Si–Mg–Cu cast alloys, Mater. Sci. Eng. A 577 (2013) 64–72.
[20] H. Okamoto, Al-Ti (Aluminum-Titanium), J. Phase Equilibria 23 (2002) 120.
[21] G. Tong, L. Dakui, W. Zuoshan, L. Xiangfa, Evolution, microhardness of ZrAlSi intermetallic and its impact on the elevated-temperature properties in Al–Si alloys, Mater. Sci. Eng. A 552 (2012) 523–529.
[22] K.E. Knipling, D.C. Dunand, Creep resistance of cast and aged Al–0.1Zr and Al–0.1Zr–0.1Ti (at%) alloys at 300–400 °C, Scr. Mater. 59 (2008) 387–390.
[23] S.H. Seyed Ebrahimi, M. Emamy, Effects of Al–5Ti–1B and Al–5Zr master alloys on the structure, hardness and tensile properties of a highly alloyed aluminum alloy, Mater. Des. 31 (2010) 200–209.
[24] S.H. Seyed Ebrahimi, M. Emamy, N. Pourkia, H.R. Lashgari, The microstructure, hardness and tensile properties of a new super high strength aluminum alloy with Zr addition, Mater. Des. 31 (2010) 4450–4456.
[25] L. Ceschini, A. Morri, A. Morri, A. Gamberini, S. Messieri, Correlation between ultimate tensile strength and solidification microstructure for the sand cast A357 aluminium alloy, Mater. Des. 30 (2009) 4525–4531.
[26] T.E. Quested, A.T. Dinsdale, A.L. Greer, Thermodynamic modelling of growth-restriction effects in aluminium alloys, Acta Mater. 53 (2005) 1323–1334.
[27] M.A. Easton, D.H. Stjohn, A model of grain refinement incorporating alloy constitution and potency of heterogeneous nucleant particles, Acta Mater. 49 (2001) 1867–1878.
[28] L. Ceschini, A. Morri, A. Morri, G. Pivetti, Predictive equations of the tensile properties based on alloy hardness and microstructure for an A356 gravity die cast cylinder head, Mater. Des. 32 (2011) 1367–1375.
[29] Z. Ma, A.M. Samuel, F.H. Samuel, H.W. Doty, S. Valtierra, A study of tensile properties in Al–Si–Cu and Al–Si–Mg alloys: effect of β-iron intermetallics and porosity, Mater. Sci. Eng.: A 490 (2008) 36–51.
[30] L. Ceschini, A. Morri, A. Morri, Estimation of local fatigue behaviour in A356-T6 gravity die cast engine head based on solidification defects content, Int. J. Cast. Met. Res. 27 (2014) 56–64.
[31] E. Ogris, A. Wahlen, H. Lüchinger, P.J. Uggowitzer, On the silicon spheroidization in Al–Si alloys, J. Light Met. 2 (2002) 263–269.
[32] V. Raghavan, Al-Er-Si (Aluminum-Erbium-Silicon), J. Phase Equilibria Diffus. 31 (2010) 44–45.
[33] W.T. Kim, B. Cantor, Heterogeneous nucleation of Al_2Cu in A1-Cu eutectic liquid droplets embedded in an Al matrix, Acta Metall. Et. Mater. 42 (1994) 3045–3053.
[34] D.T.L. Alexander, A.L. Greer, Formation of eutectic intermetallic rosettes by entrapment of liquid droplets during cellular columnar growth, Acta Mater. 52 (2004) 5853–5861.
[35] S.P. Wen, K.Y. Gao, H. Huang, W. Wang, Z.R. Nie, Precipitation evolution in Al–Er–Zr alloys during aging at elevated temperature, J. Alloy. Compd. 574 (2013) 92–97.
[36] H. Li, J. Bin, J. Liu, Z. Gao, X. Lu, Precipitation evolution and coarsening resistance at 400 °C of Al microalloyed with Zr and Er, Scr. Mater. 67 (2012) 73–76.
[37] K.E. Knipling, D.C. Dunand, D.N. Seidman, Precipitation evolution in Al–Zr and Al–Zr–Ti alloys during isothermal aging at 375–425 °C, Acta Mater. 56 (2008) 114–127.
[38] Q.G. Wang, Microstructural effects on the tensile and fracture behavior of aluminum casting alloys A356/357, Metall. Mater. Trans. A 34A (2003) 2887–2899.
[39] M. Tiryakioglu, J. Campbell, N.D. Alexopoulos, Quality indices for aluminum alloy castings: a critical review, Metall. Mater. Trans. B 40B (2009) 802–811.
[40] M. Drouzy, S. Jacob, M. Richard, Interpretation of tensile results by means of quality index and probable yield strength, AFS Int. Cast. Met. J. 5 (1980) 43–50.
[41] Aluminium and aluminium alloys castings. In: Chemical Composition and Mechanical Properties, ISO Standards, 2007.